Engineering 59 (2026) 271–286

Contents lists available at ScienceDirect

Engineering

journal homepage: www.elsevier.com/locate/eng

Research
Low Carbon Transformation for Conventional Energies—Article

Numerical Study of Heat Transfer Performance of Molten Salt-Based Nanofluid in the Novel Twisted Cloverleaf U-Tube

Yifan Gui [a], Yuanqiang Duan [a,*], Shuo Zhang [a], Yu Huang [b], Minmin Zhou [a], Lunbo Duan [a]

[a] Key Laboratory of Energy Thermal Conversion and Control, Ministry of Education, School of Energy and Environment, Southeast University, Nanjing 210096, China
[b] International Joint Research Laboratory for Energy Power Equipment Energy Conservation and Pollutant Control of Henan, Henan University of Science and Technology, Luoyang 471003, China

ARTICLE INFO

Article history:
Received 5 August 2025
Revised 22 September 2025
Accepted 16 October 2025
Available online 23 October 2025

Keywords:
Molten salt-based nanofluid
Numerical simulation
Heat transfer enhancement
Twisted cloverleaf U-tube
Multi-objective optimization

ABSTRACT

Molten salt is widely adopted in diverse thermal energy storage systems owing to its exceptional thermodynamic properties and economical cost. As a critical component in molten salt energy storage systems, the exchangers often utilize U-tube configurations for enhanced compactness, such as shell-and-tube designs. However, the high viscosity and density of molten salt can cause non-uniform flow distribution in U-tubes, posing localized overheating risks. This study proposes a heat transfer enhancement strategy applying a twisted cloverleaf U-tube in combination with molten salt-based nanofluids (MSBNs). The effects of tube geometry, operating parameters, and nanofluid thermophysical properties on flow and thermal performance were analyzed through numerical simulations. Multi-objective optimization of operating conditions was conducted using a combination of response surface method (RSM) and the non-dominated sorting genetic algorithm II (NSGA-II). Results indicate the twisted structure and nanoparticles significantly enhance heat transfer and improve temperature uniformity, however increase pressure drop. The optimal combination achieved a peak performance evaluation criterion (PEC) value of 1.21. Inlet velocity and inlet temperature influence flow and heat transfer performance additional strongly than heat flux. Optimized operating conditions yield a maximum temperature difference of 40.15 K, pressure drop of 1979.97 Pa, and average convective heat transfer coefficient of 2781.31 $W{\cdot}(m^2{\cdot}K)^{-1}$. This work provides critical guidance for the design and operational optimization of novel MSBN heat exchange tubes.

1. Introduction

Driven by the global energy transition and the pursuit of sustainable development, the global application scale of renewable energy continues to expand [1]. However, renewable energy sources are inherently characterized by intermittency, volatility, dispersion, and uncertainty [2], which pose significant challenges to the stable operation and maintenance of energy systems. Thermal energy storage (TES) technology is widely regarded as a key solution to address these challenges due to its excellent regulation and load-balancing capabilities. Common TES media include water [3], oil [4], molten salt [5], and phase change materials (PCMs) [6]. Among them, molten salt stands out in applications such as thermal power flexibility [7] and solar generation [8] owing to its advantageous properties, including high thermal conductivity, substantial specific heat capacity, excellent thermal stability, high operating temperature, and low cost. As a core component of molten salt energy storage systems, the performance of molten salt heat exchangers directly influences system efficiency and operational stability, making heat transfer enhancement design a continuous focus of research and development.

To improve structural compactness and heat transfer performance, the U-tube configuration is widely utilized in shell-and-tube heat exchangers and various thermal systems [9]. As fluid passes through the U-bend section of the tube, centrifugal force drives the fluid from the outer side of the bend toward the inner wall, thereby inducing a secondary flow perpendicular to the primary flow direction [10]. Molten salt possesses higher viscosity compared to conventional working fluids, and its density is highly sensitive to temperature changes. Consequently, when molten salt

* Corresponding author.
E-mail address: 15805174453@163.com (Y. Duan).

https://doi.org/10.1016/j.eng.2025.10.010

flows through the U-bend section, the interaction between the curvature-induced secondary flow and the buoyancy-driven natural convection can significantly influence the flow and heat transfer behavior inside the tube, potentially resulting in non-uniform heat transfer and flow distribution.

Geometric tube modifications or turbulator additions can intensify fluid disturbance and enhance heat transfer. Enhancement structures comprise internally grooved tubes, finned tubes, ribbed tubes, corrugated tubes, and twisted tubes [11–15], as well as inserts such as twisted tapes and helical wires [16–18]. The twisted structure enhances heat transfer by inducing torsional forces that promote mixing between the core and near-wall fluid regions [19], thereby attracting considerable research interest. Bhadouriya et al. [20] conducted investigations to examine the heat transfer behavior of airflow within twisted square tubes. The results indicated that this configuration exhibited enhanced heat transfer performance under laminar flow, primarily due to the induction of secondary flow phenomenon. Li et al. [21] conducted a comprehensive study on the thermal–hydraulic performance of four representative symmetric cross-sectional configurations of twisted tubes. The results indicate that, under conditions of equal cross-sectional perimeter and Reynolds numbers above 1100, the triangular-shaped twisted tube achieves the highest convective heat transfer efficiency. Eiamsa-ard et al. [22] introduced a novel ribbed twisted elliptical tube configuration. Their study revealed that the Nusselt number, friction factor, and overall performance factor of this design are 0.91–2.44, 123–12.2, and 0.85–1.32 times, respectively, compared to those of a smooth circular tube. Wang et al. [23] introduced a helical twisted tube design, which effectively combines helical and twisted structural features to generate intensified secondary flow within the tube, thereby significantly improving convective heat transfer performance. Han et al. [24] established an entropy balance model for solar salt heat transfer in elliptical twisted tubes and employed multi-objective optimization to enhance thermal–hydraulic performance.

In addition to optimizing the heat exchange tube configuration, the incorporation of nanoparticles into molten salt to form molten salt-based nanofluids (MSBNs) offers a promising strategy for enhancing heat transfer performance. Ying et al. [25] demonstrated that under non-uniform heat flux boundary conditions, an Al_2O_3/Hitec nanofluid with a nanoparticle mass fraction of 0.063% can enhance the Nusselt number by up to approximately 6.90%. In a subsequent investigation [26], they reported that MSBNs exhibit improved heat transfer performance in tubes containing porous media, as compared to pure molten salt flowing through smooth tubes. Kaood et al. [27] found that the type of molten salt constitutes the MSBN has a greater impact on exergy than the type of nanoparticles. The nanofluid based on Hitec molten salt can increase energy utilization efficiency by up to 42.0% at most. Zhang et al. [28] demonstrated that the addition of SiO_2 particles to quaternary salts can increase the heat transfer coefficient by up to 22.34% compared to the pure salts. Nevertheless, current research efforts mainly concentrate on the development of MSBNs with enhanced thermophysical and chemical properties, whereas investigations into their heat transfer and flow behavior remain limited.

The review of existing literature indicates that most studies on heat transfer enhancement in molten salt and MSBNs have primarily concentrated on straight tubes, with limited investigations addressing the flow and heat transfer characteristics, as well as structural optimization of both smooth and modified U-tube configurations. In this study, a novel heat transfer enhancement strategy is proposed by integrating a twisted cloverleaf U-tube (TCUT) configuration with MSBNs. The influence of the twisted structure, nanoparticle properties, inlet conditions, and heat flux on the flow and heat transfer characteristics is systematically investigated through numerical simulations. After determining the optimal parameters of the nanoparticles, the optimization method based on the response surface method (RSM) and non-dominated sorting genetic algorithm II (NSGA-II) was established to optimize the operational parameters to achieve resulting in substantial heat transfer improvement while maintaining a low pressure drop.

2. Research methods

2.1. Physical model

The structural configuration of the TCUT is presented in Fig. 1. The U-tube consists of an inlet section, a bend section, and an outlet section. Both the inlet and outlet straight sections have an identical length (L) of 600 mm. The U-bend section has a bending radius (D) of 150 mm. The tube diameter (d), applicable to both the smooth tube and TCUT, is 30 mm. The opening radius (r_1) and transition radius (r_2) are each 3 mm. The twist pitch (P) is set at 287.1 mm.

2.2. Mathematical model

2.2.1. Governing equation

The numerical simulation is based on the following assumptions: ① Viscous dissipation and thermal radiation effects are neglected, and only convective heat transfer is considered; ② the fluid inside the tube is assumed to be a continuous, incompressible Newtonian fluid with no phase change; ③ the tube wall thickness is ignored, with no-slip boundary conditions applied at the wall surface and a uniform heat flux imposed on the outer surface of the tube; ④ gravitational effects are included, with an acceleration of –9.81 $m{\cdot}s^{-2}$ applied along the z-axis.

In this study, the Reynolds number Re of the fluid within the pipe exceeds 4000 in all cases. To accurately simulate the flow and heat transfer characteristics, the realizable k–ε turbulence model [29] was employed, which is widely used in pipe flow simulations involving elbows [30]. The finite volume method was applied to discretize the governing equations. The three-dimensional Navier–Stokes equations are expressed as follows:

Continuity equation:

$$\frac{\partial(\rho u_i)}{\partial x_i} = 0 \tag{1}$$

Momentum equation:

$$\frac{\partial(\rho u_i u_j)}{\partial x_i} = -\frac{\partial p}{\partial x_i} + \frac{\partial}{\partial x_j}((\mu + \mu_t)(\frac{\partial u_i}{\partial x_j} + \frac{\partial u_j}{\partial x_i})) \tag{2}$$

Energy equation:

$$\frac{\partial(\rho u_i T)}{\partial x_i} = \frac{\partial}{\partial x_i}(\frac{\mu}{Pr} + \frac{\mu_t}{Pr_t})\frac{\partial T}{\partial x_i} \tag{3}$$

In the realizable k–ε turbulence model, the transport equations for turbulent kinetic energy (TKE) k and turbulent dissipation rate ε are expressed as follows.

Kinetic energy equation (k):

$$\frac{\partial(\rho u_i k)}{\partial x_i} = \frac{\partial}{\partial x_i}((\mu + \frac{\mu_t}{\sigma_k})\frac{\partial k}{\partial x_i}) + \Gamma - \rho\varepsilon \tag{4}$$

Dissipation rate equation (ε):

$$\frac{\partial(\rho u_i \varepsilon)}{\partial x_i} = \frac{\partial}{\partial x_i}((\mu + \frac{\mu_t}{\sigma_\varepsilon})\frac{\partial k}{\partial x_i}) + c_1\Gamma\varepsilon - \rho c_2\frac{\varepsilon^2}{k + \sqrt{v\varepsilon}} \tag{5}$$

where ρ denotes density, u represents velocity, x denotes the position vector, p signifies pressure, T indicates temperature, μ stands for viscosity, μ_t denotes turbulent viscosity, Pr represents the

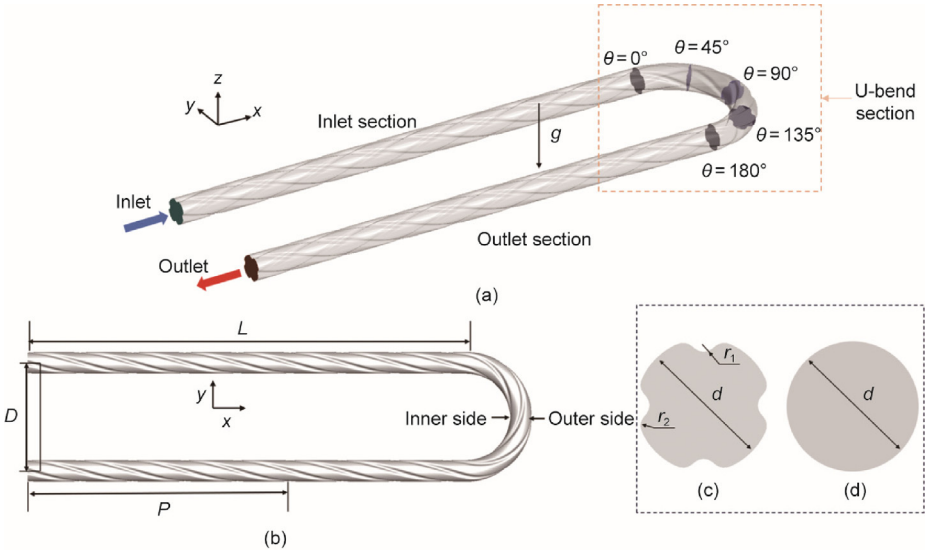

Fig. 1. The geometric model of the U-tube: (a) three-dimensional view, (b) top view, (c) TCUT cross-section, (d) smooth tube cross-section. θ: bending angle; g: gravitational acceleration.

Prandtl number, while Pr_t, σ_k, and σ_ε correspond to the Prandtl numbers for temperature, TKE, and turbulent dissipation rate, respectively. v is the molecular kinematic viscosity, c_1 is a variable production coefficient, and c_2 is a constant destruction coefficient. The subscripts i and j respectively represent the spatial direction and ummation over all spatial directions. Γ represents TKE, and the expression is as follows:

$$\Gamma = \mu_t\left(\frac{\partial u_i}{\partial x_j} + \frac{\partial u_j}{\partial x_i}\right)\frac{\partial u_i}{\partial x_i} \tag{6}$$

To ensure high computational accuracy, the momentum and energy equations are discretized using a second-order upwind scheme, while the pressure–velocity coupling is addressed through the SimpleC algorithm. The computation is deemed convergent when the relative residual of the continuity equation drops below 10^{-5}, and the residuals of the other governing equations fall below 10^{-7}.

2.2.2. Thermal properties and boundary conditions

Hitec salt (53 wt% KNO_3 + 40 wt% $NaNO_2$ + 7 wt% $NaNO_3$) is employed as the basic fluid of the MSBN in this study. The thermophysical properties of Hitec salt are expressed as temperature-dependent functions, and the calculation methods for density (ρ), specific heat capacity (c_p), thermal conductivity (λ), and dynamic viscosity (μ) [31] are presented as follows:

$$\rho = 2084 - 0.74T \tag{7}$$

$$c_p = 1560 \tag{8}$$

$$\lambda = 0.411 + 4.36 \times 10^{-4}T - 1.514 \times 10^{-6}T^2 \tag{9}$$

$$\mu = 10^{2.737}T^{-2.104} \tag{10}$$

Assuming the uniform dispersion of nanoparticles within the base fluid and the attainment of thermal equilibrium between nanoparticles and molten salt, the nanofluid can be treated as a single-phase fluid. The methodology for calculating the thermophysical properties of MSBNs [32,33] is presented as follows:

$$\rho_{nf} = (1-\varphi)\rho_{bf} + \rho_{np} \tag{11}$$

$$(\rho c_p)_{nf} = (1-\varphi)(\rho c_p)_{bf} + (\rho c_p)_{np} \tag{12}$$

$$k_{nf} = \frac{k_{np} + 2k_{bf} - 2\varphi(k_{bf} - k_{np})}{k_{np} + 2k_{bf} + \varphi(k_{bf} - k_{np})} \tag{13}$$

$$\mu_{nf} = \frac{\mu_{bf}}{(1-\varphi)^{2.5}} \tag{14}$$

where φ means the volume fraction of nanoparticles. Subscripts nf, bf, and np represent the thermophysical properties of the nanofluid, base fluid, and nanoparticles, respectively.

The study focuses on three types of nanoparticles, namely SiO_2, Al_2O_3, and Cu, with the thermophysical properties shown in Table 1 [34–36].

The boundary conditions are configured as follows:

(1) Inlet condition: A mass flux inlet boundary condition is applied, with values determined by the inlet Reynolds number (Re) and inlet temperature (T_{in}). The Re range is specified as 4 000–12 000, and the T_{in} range is set 473.15–573.15 K.

(2) Outlet condition: A pressure outlet boundary condition is implemented.

(3) Tube wall: A constant heat flux boundary condition is assigned, with the heat flux (q) ranging from 10 to 110 kW·m^{-2}.

2.3. Parameter definitions

The mathematical expressions for the Re, average convective heat transfer coefficient (h), pressure drop (ΔP), Nusselt number (Nu), and friction factor (f) are as follows:

$$Re = \frac{Gd}{\mu} \tag{15}$$

$$h = \frac{q}{T_w - T_f} \tag{16}$$

Table 1
Thermal properties of nanoparticles [34–36].

Nanoparticle	Density (kg·m^{-3})	Specific heat capacity (J·(kg·K)$^{-1}$)	Thermal conductivity (W·(m·K)$^{-1}$)
SiO_2	2200	703	1.2
Al_2O_3	3600	450	40.0
Cu	8954	383	400.0

$$\Delta P = P_{in} - P_{out} \tag{17}$$

$$Nu = \frac{hd}{k} \tag{18}$$

$$f = \frac{\Delta P d}{2\rho u^2 l} \tag{19}$$

where G represents the mass flux. T_w and T_f denote the mean temperatures of the wall surface and the fluid, respectively. P_{in} and P_{out} denote the pressure at the inlet and outlet of the pipe. l is the length of the pipeline.

Multiple cross-sections are established perpendicular to the main flow direction. The local convective heat transfer coefficient (h_i) and the local circumferential heat transfer uniformity index (σ_i) at each cross-section are calculated as follows:

$$h_i = \frac{q}{T_{wi} - T_{fi}} \tag{20}$$

$$\sigma_i = \frac{T_{wi}^{max} - T_{wi}^{min}}{q} \tag{21}$$

where T_{wi} and T_{fi} represent the average wall temperature and average fluid temperature of the cross-section, respectively. T_{wi}^{max} and T_{wi}^{min} respectively represent the highest and lowest wall temperatures at tube cross-section.

The calculation methodology for the comprehensive performance evaluation criterion (PEC) [37] is as follows:

$$PEC = \frac{\left(\frac{h}{h_0}\right)}{\left(\frac{\Delta P}{\Delta P_0}\right)^{\frac{1}{3}}} \tag{22}$$

where h_0 and ΔP_0 represent the convective heat transfer coefficient and pressure drop of pure Hitec molten salt flowing in a smooth U-tube, respectively. The PEC is defined as the ratio of the average convective heat transfer coefficient to the cube root of the pressure drop before and after the implementation of heat transfer enhancement measures. A PEC value greater than 1 indicates the effectiveness of the enhancement measures, with higher values reflecting superior performance improvement.

The field synergy angle [38] is expressed as:

$$\beta = \arccos\frac{U \cdot \nabla T}{|U||\nabla T|} \tag{23}$$

where U and ∇T represent the velocity vector and temperature gradient, respectively.

3. Grid independence test and model validation

3.1. Grid independence

In this study, unstructured meshes were generated throughout the entire computational domain, with local mesh details presented in Fig. 2(a). A boundary layer mesh consisting of 20 layers was constructed near the wall surface, where the first layer thickness was set to 0.015 mm to ensure $y+ < 1$. Four different mesh configurations with varying numbers of cells were tested under the boundary conditions T_{in} = 523.15 K, G = 745.36 kg·s^{-1}, and q = 60 kW·m^{-2} to verify mesh independence. The results are shown in Fig. 2(b) and Table 2. The deviations in T_w and ΔP between mesh configuration 2 and mesh configuration 4 were only 0.064% and 0.608%, respectively. Taking both computational accuracy and efficiency into account, mesh configuration 2 was selected for subsequent simulations. Using the same approach, the number of grids for the smooth tube was determined to be 2 072 742.

3.2. Numerical simulation accuracy validation

Before conducting numerical calculations, it is imperative to validate the accuracy of the model. To validate the accuracy of the flow and heat transfer simulations in the bend section of the U-tube, the Nusselt number (Nu) and friction factor (f) obtained from the smooth U-tube simulations were compared against the correlations proposed by Rogers and Mayhew [39] (Eq. (24)) and Schmidt [40] (Eq. (25)), respectively. As shown in Fig. 3 [39,40], the deviations of the simulated Nu and f values from those predicted by the correlations were within 12.69% and 8.42%.

$$Nu = 0.023 Re^{0.85} Pr^{0.4} (d/D)^{0.1} \tag{24}$$

$$f = [1 + 0.14(d/D)^{0.97} \cdot Re^{[1-0.644(d/D)^{0.312}]}]\frac{64}{Re} \tag{25}$$

To validate the accuracy of the mixed convection heat transfer simulation for molten salt, a geometric model was constructed with dimensions matching those of the horizontal square tube used in the experiments conducted by Chen et al. [41]. The square tube employed in their study had a length of 1000 mm and a width of 19 mm, with only the bottom surface exposed to uniform heat flux. Fig. 4 [41] illustrates the comparison between the simulation results and the calculation results of Eq. (26) fitted from experimental data. The maximum deviation does not exceed 6.62%, which indicates that the numerical results match well with the measured values.

$$Nu = 4.78 Re^{0.269} Pr^{0.21} Gr^{0.07} (D/L)^{0.36} \tag{26}$$

Finally, to validate the accuracy of molten salt nanofluid flow in uniformly heated tubes, a physical model consistent with the experimental setup conducted by Ho and Pan [42] was established for computational comparison. In their experiments, four types of nanofluids were tested, each prepared by adding Al_2O_3 particles at different mass fractions to Hitec molten salt. For the purpose of validation in this study, the heat transfer correlation (Eq. (27)) for nanofluid flow in uniformly heated pipes containing a 0.25% mass fraction of Al_2O_3 was selected. The comparative results, as shown in Fig. 5, demonstrate that the deviation between the simulation data and the correlation remains within 9%, indicating that the numerical model achieves a reasonable level of accuracy.

$$Nu = 1.116\left(4.364 + \frac{0.092 x_L^*}{1 + 0.053 (x_L^*)^{-2/3}}\right) \tag{27}$$

where x_L^* is a dimensionless length, defined as $x_L^* = \frac{L}{Pr \cdot Re \cdot D}$.

4. Results and discussion

4.1. Effect of U-tube structure on the overall flow and heat transfer characteristics

Fig. 6 illustrates the wall temperature distribution in smooth and twisted tubes under the conditions of Re = 6000, q = 85 kW·m^{-2}, T_{in} = 523.15 K, and φ = 0. In the smooth U-tube, distinct zones of elevated temperatures are observed on the inner side wall at the U-bend section. The maximum temperatures significantly exceed 630 K, accompanied by considerable circumferential temperature variations. At the outlet section, the temperature peak gradually shifts toward the upper wall and decreases in magnitude due to the buoyancy effect resulting from the reduction in molten salt density with increasing temperature. Excessive temperature gradients may give rise to significant thermal stresses, which could compromise the operational safety of the heat exchanger, while overheating conditions may also lead to molten salt decomposition. In contrast, the peak temperature at the inner wall of the TCUT bend is

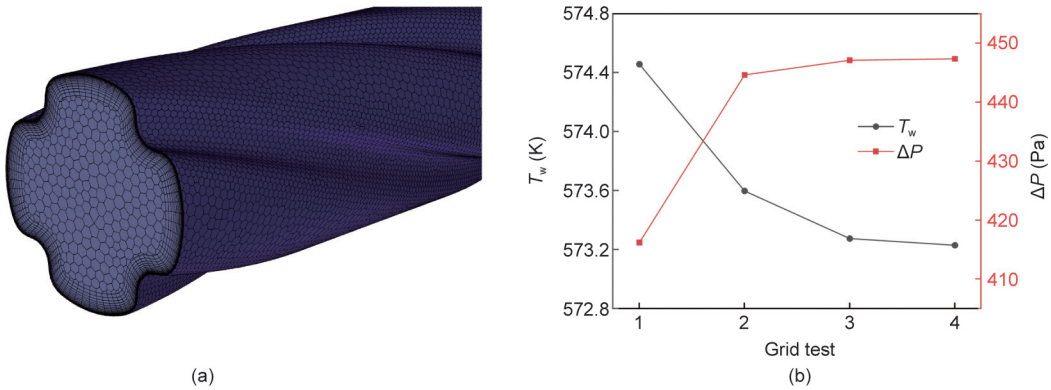

Fig. 2. Grid independence of the TCUT: (a) mesh schematic, (b) grid independence test.

Table 2
Grid verification error analysis of the TCUT and smooth tube.

Configuration	Tube style	Grid number	T_w (K)	Error$_1$ (%)	ΔP (Pa)	Error$_2$ (%)
1	TCUT	614 568	574.46	0.214	416.20	6.966
2		2 988 409	573.60	0.064	444.65	0.608
3		4 367 949	573.26	0.008	447.13	0.053
4		5 094 294	573.23	0	447.37	0
5	Smooth tube	628 976	559.11	0.130	416.20	0.230
6		1 094 686	573.60	0.003	444.65	0.238
7		2 072 742	573.28	0.005	447.13	0.110
8		3 692 846	573.23	0	447.37	0

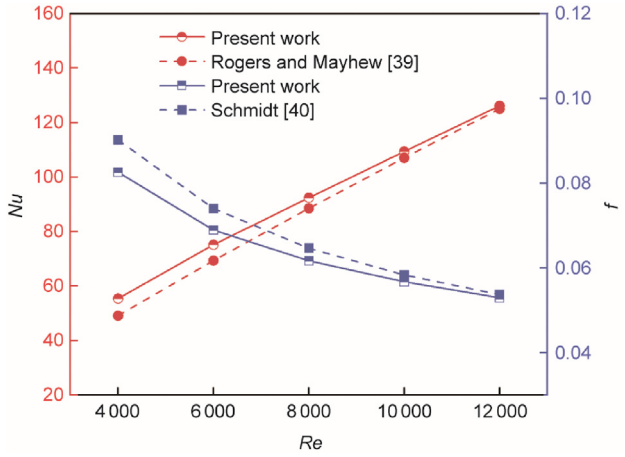

Fig. 3. Model verification: U-tube.

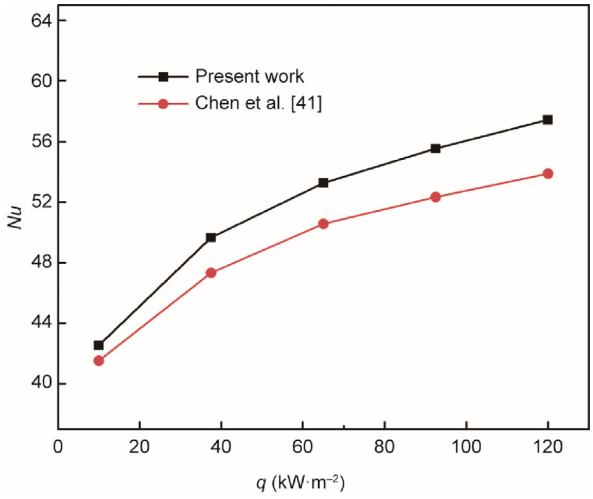

Fig. 4. Model verification: mixed convection heat transfer of molten salt.

considerably lower, with a markedly improved uniformity in the wall temperature distribution.

Fig. 7 illustrates the temperature and streamline distributions across various cross-sections of the U-bend segment and the downstream smooth tube and TCUT, under the conditions of Re = 6000, q = 85 kW·m^{-2}, T_{in} = 523.15 K, and φ = 0. In the smooth tube, a distinct temperature peak is observed on the upper side of the bend section from 45° to 180°, resulting from the combined effects of centrifugal and buoyancy forces. To facilitate a more intuitive comparison, the average temperatures at different interfaces of smooth tube and TCUT were calculated based on the temperature field distribution shown in Fig. 7. And the detailed results are presented in Fig. S1 in Appendix A. Also, the average temperature distributions at smooth tube and twisted tube are also provided in Table 2. In contrast, the TCUT demonstrates a considerable expansion of the medium-to-low temperature regions, while maintaining most of the fluid temperature below 600 K. The streamline distribution reveals the formation of two secondary vortices within the bend segment of the smooth tube. In the U-bend section of the TCUT, the combined action of torsional forces induced by the twisted structure and centrifugal forces generates one to two additional secondary vortices, which promote the migration of high-temperature fluid near the inner wall toward the central region of the tube. This phenomenon significantly enhances the mixing between the central and near-wall fluid regions, thereby disrupting both the velocity and thermal boundary layers.

TKE is defined as half the sum of the mean square values of the fluctuating velocity components in three orthogonal directions per unit mass of fluid. It serves as a key physical parameter for characterizing turbulence intensity. Fig. 8 illustrates the distribution of

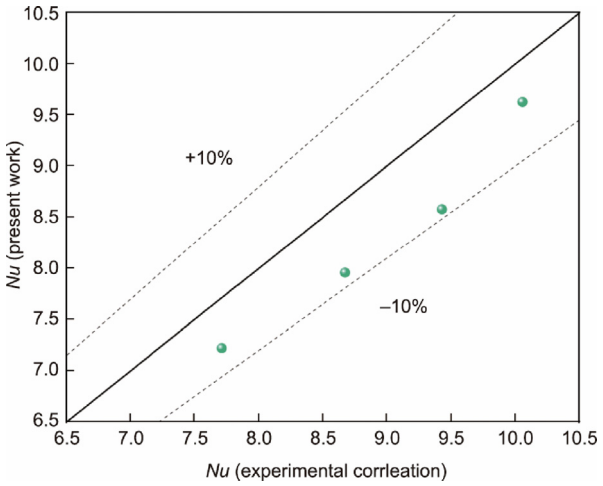

Fig. 5. Model verification: convection heat transfer of MSBN.

TKE across several cross-sectional planes from the inlet of the U-bend section to the outlet section, under the conditions of Re = 6000, q = 85 kW·m^{-2}, T_{in} = 523.15 K, and φ = 0. In the smooth tube, the secondary flow induced by centrifugal and buoyancy forces causes the peak radial velocity to shift toward the lower outer side of the bend, resulting in higher fluid velocities in the outer region compared to the inner region (Fig. 9(a)). Consequently, the velocity gradient near the wall in the outer region is greater than that in the inner region. Given that the velocity gradient significantly influences the magnitude of TKE, the TKE near the wall in the inner bend region is markedly reduced, indicating weaker turbulence and diminished mixing in this area. The twisted structure substantially enhances the overall level of TKE and effectively reduces the low-TKE zone in the inner bend by increasing the near-wall velocity gradient. As illustrated in Fig. 9(b), at the θ = 180° cross-sectional plane, the maximum TKE in the twisted tube is significantly higher than that in the smooth tube. This is attributed to the strong disturbance in the velocity field caused by the interaction of multiple vortices with different orientations within the twisted tube bend, which intensifies local shear stress and velocity gradients. However, the increase in TKE also implies greater energy dissipation, necessitating an assessment of whether the improvement in heat transfer performance justifies the associated energy losses.

The previous analysis of the temperature distribution shows that due to the combined effects of centrifugal and buoyancy forces, the peak temperature on the wall of the smooth U-tube occurs on the inner side of the bend in its upper section. Therefore, the axial cross-section at z = 0.003 m is selected for velocity distribution analysis, as shown in Fig. 10. It can be observed that the velocity distribution in the inlet section of the smooth tube remains relatively uniform. However, upon entering the U-bend section, the strong centrifugal force leads to the formation of a high-velocity region on the outer side and a low-velocity region on the inner side. This phenomenon becomes more pronounced in the outlet section. In contrast, the twisted tube exhibits significantly improved velocity uniformity, particularly enhancing the velocity magnitude on the inner side of the U-bend section and the outlet section.

Guo et al. [38] proposed the field synergy angle principle, which states that heat transfer efficiency is not only determined by the magnitudes of the flow velocity and temperature gradient, but more critically by the angular relationship between the velocity vector and the temperature gradient vector. The field synergy angle β ranges from 0° to 90°, with smaller values indicating superior heat transfer performance. Fig. 11 presents the distribution of the field synergy angle on the axial cross-sectional plane at z = 0.003 m for both smooth U-tubes and twisted tubes. In the inlet section, the field synergy angle at the fluid center is relatively small. As the fluid enters the U-bend segment, the angle gradually approaches its minimum value and spreads toward both sides. The unique structure of the twisted tube significantly reduces the field synergy angle, particularly within the U-bend segment and in the downstream region near the tube wall. This indicates that the introduction of torsional forces, in combination with centrifugal forces within the U-bend section, enhances the synergistic interaction between the velocity vector and the temperature gradient.

4.2. Effect of thermophysical properties and operating conditions on overall thermal–hydraulic performance

4.2.1. Effect of nanoparticle types and Reynolds number

To determine the optimal type of nanoparticles, this section analyzes the heat transfer performance and pressure drop characteristics of pure Hitec molten salt and MSBN containing 3% of different nanoparticles in both smooth and twisted U-tubes, under the conditions of T_{in} = 523.15 K and q = 60 kW·m^{-2}. As illustrated in Figs. 12(a) and (b), increasing the Re, implementing a twisted tube structure, and incorporating nanoparticles all contribute to an enhancement in the h while simultaneously increasing the ΔP. At higher Re, the effects of the twisted structure and nanoparticle addition on both h and ΔP become stronger. Notably, when 3% SiO_2 MSBN flows through the twisted tube, ΔP increases by

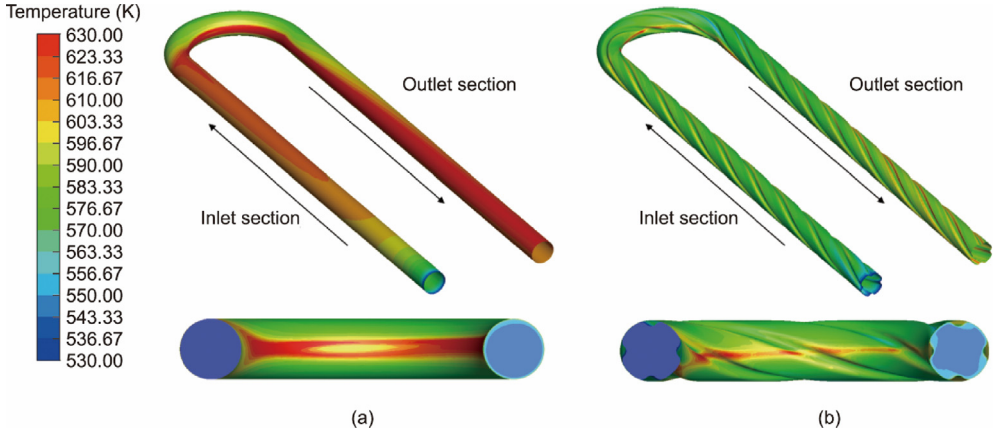

Fig. 6. The temperature contours on the tube wall: (a) smooth tube, (b) TCUT.

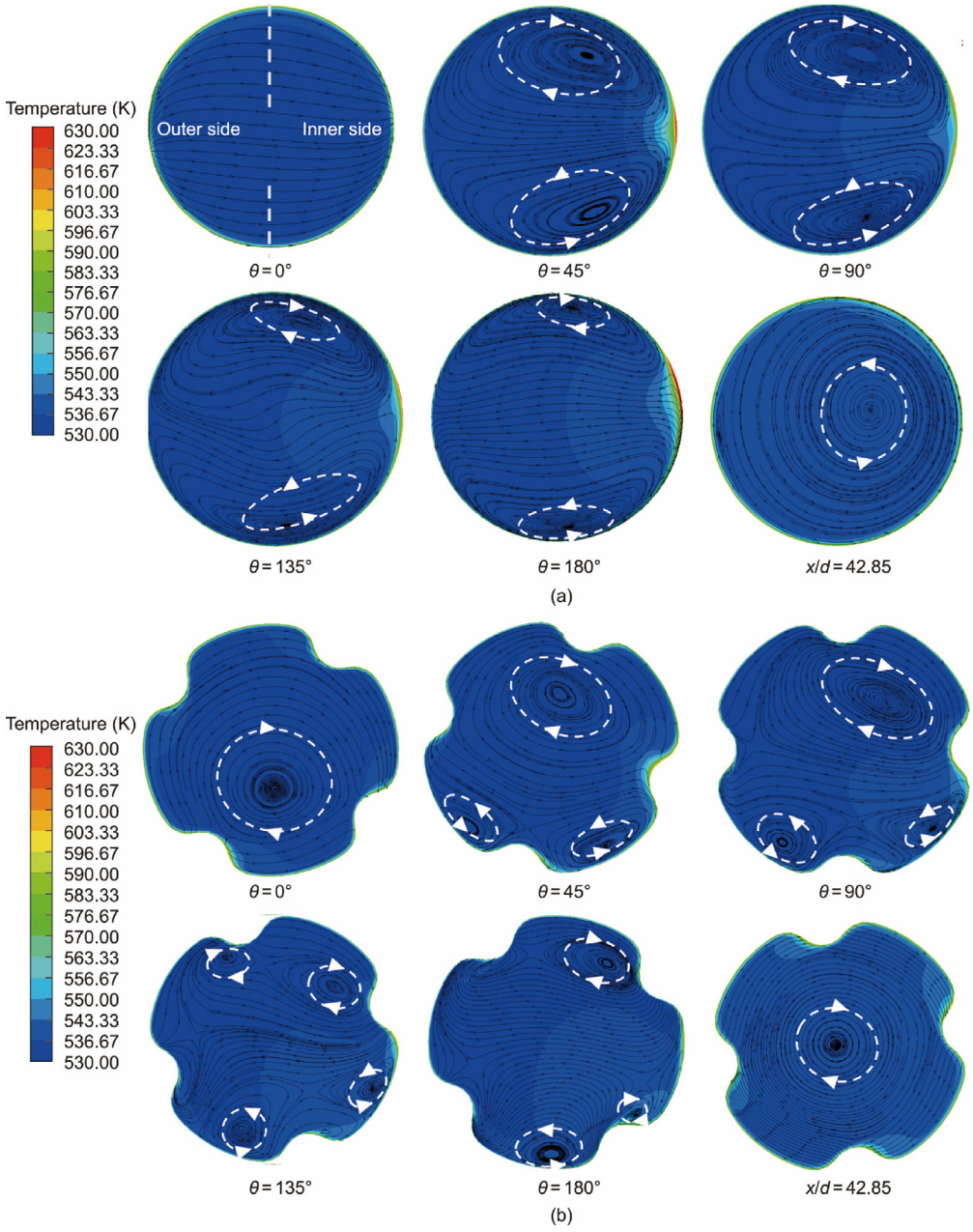

Fig. 7. Temperature and flow field distributions at different cross-sections: (a) smooth tube, (b) twisted tube.

452.91 Pa as *Re* increases from 4000 to 6000, and by 780.42 Pa as *Re* increases from 10 000 to 12 000, indicating that the rate of ΔP increase accelerates with rising *Re*.

The addition of nanoparticles significantly enhances heat transfer performance, primarily due to three mechanisms: ① The intrinsic thermal conductivity of nanoparticles exceeds that of the base molten salt, and their uniform dispersion directly improves the effective thermal conductivity of the nanofluid; ② the Brownian motion of nanoparticles induces microscale convection in the surrounding molten salt, thereby enhancing fluid mixing; ③ the random motion of nanoparticles continuously disturbs the viscous sublayer near the wall, further reducing the thermal boundary layer thickness [43].

The enhancement effect of different nanoparticle types on the convective heat transfer coefficient follows the ascending order: Cu > Al_2O_3 > SiO_2. Compared to the smooth tube with pure Hitec salt, the twisted tube with 3% Cu MSBN increases *h* by 22.57%–34.53%. The heat transfer performance of nanofluids is positively correlated with the thermal conductivity of the incorporated nanoparticles. Since Cu exhibits the highest thermal conductivity, the thermal conductivity of Cu-based nanofluids surpasses that of other nanofluids at the same φ. At higher *Re* values, the increased frequency and velocity of nanoparticle motion further amplify the heat transfer enhancement effect. As shown in Fig. 12(b), the pressure drop enhancement effect of nanoparticles follows the ascending order: SiO_2 > Al_2O_3 > Cu. Compared to the smooth tube with pure Hitec salt, the twisted tube with 3 vol% SiO_2 MSBN increases ΔP by 63.91%–70.11%. At identical *Re* values, the ΔP of nanofluids is inversely correlated with the density of the incorporated nanoparticles. Since the SiO_2 MSBN has the lowest density, it achieves the highest flow velocity under the same *Re*, consequently resulting in the maximum ΔP.

Fig. 12(c) presents that the PEC decreases with increasing *Re*. For the configuration of twisted tubes combined with 3% Cu MSBN,

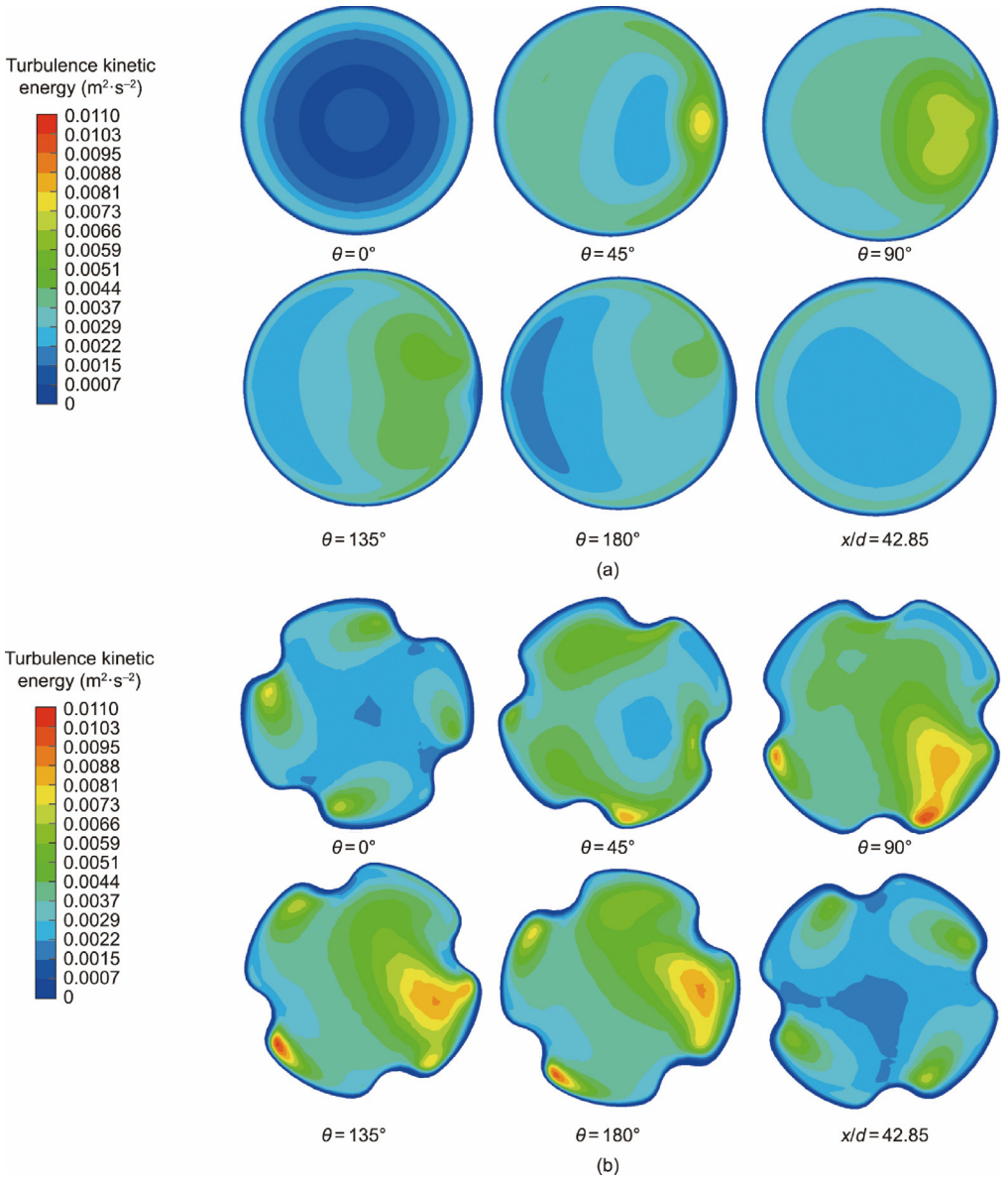

Fig. 8. Turbulence kinetic energy distributions at different cross-sections: (a) smooth tube, (b) twisted tube.

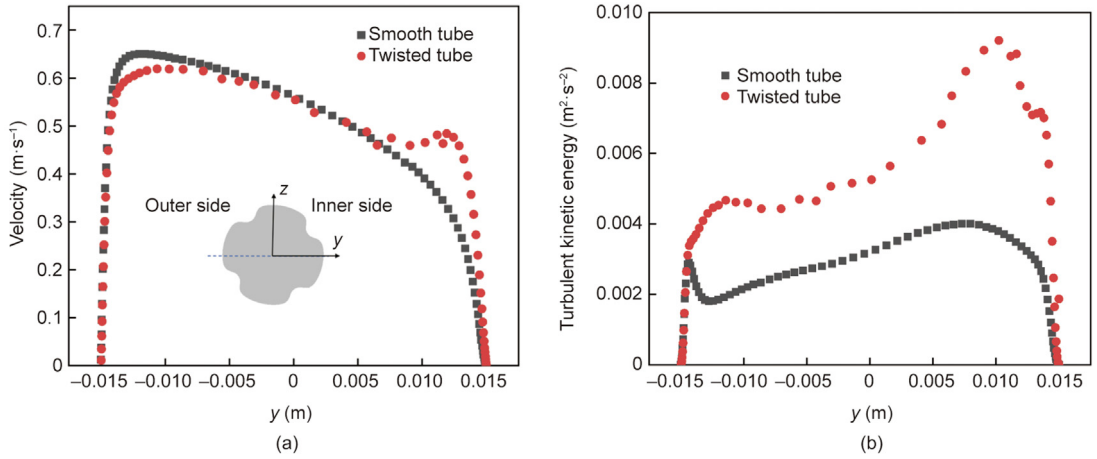

Fig. 9. (a) Velocity distribution along the *y*-axis in the *x*-direction and (b) the TKE distribution at the cross-section of θ = 180°.

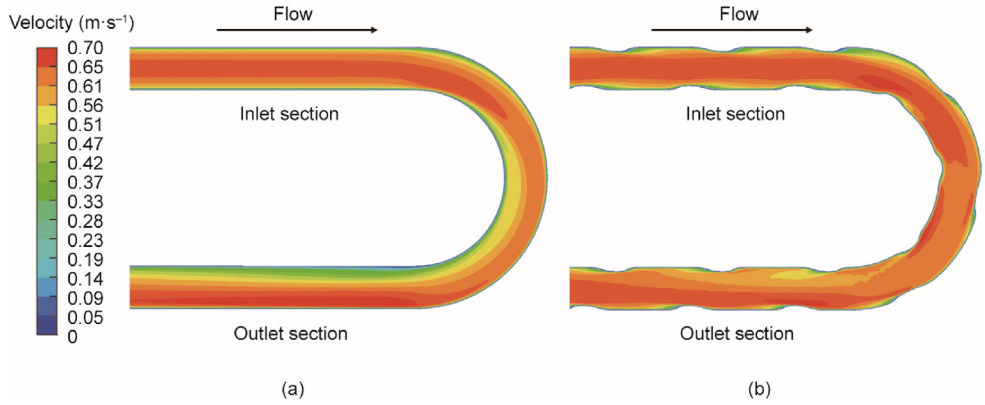

Fig. 10. Velocity distribution at the cross-section of z = 0.003 m: (a) smooth tube, (b) twisted tube.

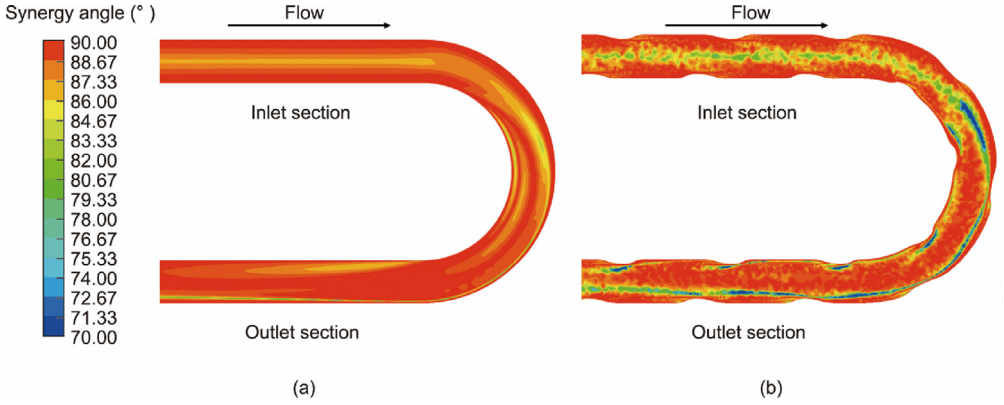

Fig. 11. Field synergy angle distribution at the cross-section of z = 0.003 m: (a) smooth tube, (b) twisted tube.

when *Re* increases from 4 000 to 12 000, PEC decreases from 1.17 to 1.07. Compared with smooth tubes, the PEC of the twisted structure remains greater than 1, indicating that the enhancement in heat transfer performance across different inlet flow rates outweighs the corresponding increase in ΔP. The addition of nanoparticles other than SiO_2 further improves the PEC. The ranking of PEC for different nanofluids follows the order: Cu > Al_2O_3 > SiO_2. Compared with the configuration of smooth tubes combined with pure Hitec salt, the configuration of twisted tubes combined with 3% Cu MSBN achieves a maximum PEC of 1.17. The PEC of SiO_2 MSBN is lower than that of pure Hitec salt, indicating that the pressure drop associated with the addition of SiO_2 nanoparticles exceeds the improvement in heat transfer performance. Because Cu MSBN exhibits the highest PEC, it is selected for subsequent investigation.

4.2.2. Effect of inlet temperature and volume fraction of nanoparticles

The inlet temperature of MSBN and the volume fraction of nanoparticles are both important factors affecting the heat transfer performance. Figs. 13(a) and (b) present the effects of different T_{in} on the h and ΔP for pure Hitec salt and Cu MSBN with φ of 1%, 3%, and 5% flowing through two types of U-tubes, under conditions of *Re* = 6000 and q = 60 kW·m^{-2}. As shown in Fig. 13(a), h decreases with increasing T_{in}, and the higher φ, the greater the value of h. When T_{in} increases from 473.15 to 573.15 K, the h of the smooth tube with pure Hitec salt and the twisted tube with 5 % Cu MSBN decreases from 1550.31 and 2172.68 W·(m^2·K)$^{-1}$ to 1110.29 and 1515.93 W·(m^2·K)$^{-1}$, respectively. This is attributed to the fact that both the thermal conductivity and viscosity of Hitec salt decrease with increasing temperature. At the same *Re*, a fluid with lower T_{in} exhibits a higher flow rate, and both the higher thermal conductivity and flow rate contribute to an increase in h.

As illustrated in Fig. 13(b), ΔP decreases with increasing T_{in}. Notably, for the smooth tube with pure Hitec salt and the twisted tube with 5% Cu MSBN, when T_{in} increases from 473.15 to 498.15 K, ΔP decreases by 532.34 and 855.01 Pa, respectively. When T_{in} increases from 548.15 to 573.15 K, ΔP decreases by only 110.85 and 177.71 Pa, respectively. This indicates that the rate of ΔP reduction significantly slows down with increasing temperature, which is due to the decreasing rate of dynamic viscosity reduction of the molten salt as temperature rises.

Fig. 13(c) further illustrates that the PEC increases with φ. At T_{in} = 473.15 K, as φ in the twisted tube increases from 0 to 5%, the PEC rises from 1.09 to 1.20. Moreover, the PEC decreases with the elevation of T_{in}. Specifically, at φ = 5%, when T_{in} increases from 473.15 to 573.15 K, the PEC declines from 1.20 to 1.17, indicating that the influence of φ on PEC is significantly greater than that of T_{in}.

4.2.3. Effect of heat flux

Load variations in energy storage systems induce dynamic fluctuations in heat flux on molten salt heat exchanger, therefore it is essential to investigate the flow and heat transfer characteristics of MSBN under varying heat flux conditions. Figs. 14(a) and (b) present the influence of varying q on the h and ΔP of pure Hitec salt and Cu MSBN with φ of 1%, 3%, and 5% in two types of U-tubes, under conditions of *Re* = 6000 and T_{in} = 523.15 K. It is evident that increasing q has a negligible effect on h when Hitec salt flows through the smooth tube. However, in the twisted tube configuration, h increases with rising q. Specifically, for the case of 5% Cu MSBN flowing through the twisted tube, when q increases from 10 to 110 kW·m^{-2}, h increases by 38.85 W·(m^2·K)$^{-1}$. This phenomenon can be attributed to the fact that higher q induces an

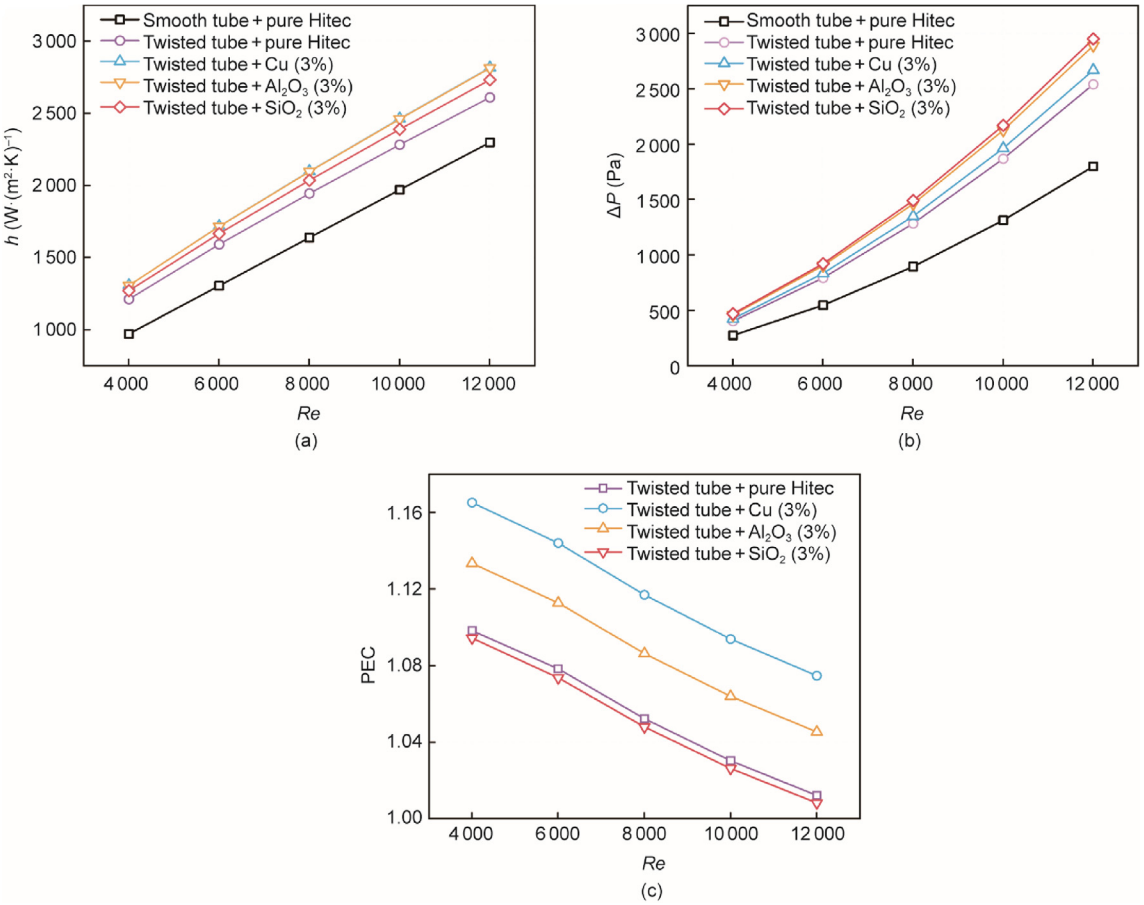

Fig. 12. Variation of (a) h, (b) ΔP, and (c) PEC with Re for different types of MSBN in smooth and twisted tubes.

increased temperature gradient on the corrugated walls of the twisted tube, where the synergistic effect of density variations in the molten salt and the twisted structure further enhances secondary flow, disrupts the thermal boundary layer, and thereby intensifies heat transfer. As shown in Fig. 14(b), compared to h, q has a more pronounced effect on ΔP. For the case of 5% Cu MSBN flowing through the twisted tube, when q increases from 10 to 110 kW·m^{-2}, ΔP decreases by 96.5 Pa, primarily due to the high q reducing the viscosity of the molten salt near the tube wall.

Fig. 14(c) presents the influence of varying q on the PEC. The PEC demonstrates a slight decreasing trend as q increases, with the effect of q on PEC becoming more significant at higher φ. When q increases from 10 to 110 kW·m^{-2}, the PEC for the 5% SiO_2 MSBN in the twisted tube configuration decreases from 1.89 to 1.83. This suggests that, in comparison to the T_{in} and Re, variations in q have a relatively minor impact on the overall PEC.

4.3. Local convection heat transfer characteristics of MSBN in U-tube

4.3.1. Effect of twisted structure and nanoparticles

The analysis of variations in local heat transfer coefficients (h_i) and temperature non-uniformity index (σ_i) along the tube may provide more comprehensive insights into the influence of U-bend section and other factors on local heat transfer characteristics. Figs. 15(a) and (b) present the variations of the h_i and the σ_i along the main flow direction for pure Hitec salt in two different U-tube configurations, as well as for MSBN with varying φ in twisted U-tubes, under conditions of q = 60 kW·m^{-2}, T_{in} = 523.15 K, and Re = 6000. As shown in Fig. 15(a), h_i decreases rapidly from the inlet due to the thin thermal boundary layer in the entrance region and stabilizes within a consistent range upon entering the fully developed section. A significant increase in h_i is observed when the flow enters the U-bend section, followed by a gradual decline to a stable level in the outlet section. Fig. 15(a) reveals that the increase in h_i within the U-bend section of the twisted tube is significantly greater than that in the smooth tube. When Hitec salt transitions from the inlet section to the U-bend, h_i in the smooth and twisted tubes increases from 1158.64 and 1374.86 W·(m^2·K)$^{-1}$ to 1573.86 and 2040.06 W·(m^2·K)$^{-1}$, respectively. This demonstrates that the enhanced heat transfer effect induced by the secondary flow resulting from the combined action of centrifugal and torsional forces in the U-bend section of the twisted tube is significantly greater than that in the smooth tube. Furthermore, the rate of increase in h_i within the U-bend section is positively correlated with the nanoparticle concentration, with maximum h_i values of 2091.78610, 2198.154580, and 2309.06855 W·(m^2·K)$^{-1}$ observed for 1%, 3%, and 5% Cu MSBN flowing in the twisted tube, respectively. This is attributed to the strong secondary flow in the U-bend section increasing the collision probability of nanoparticles, thereby further enhancing the heat transfer intensity.

Fig. 15(b) illustrates that two σ_i peaks are generated in the U-bend section of the smooth tube. In contrast, the twisted structure increases σ_i in the inlet section but effectively eliminates the σ_i peak at the outlet of U-bend section. Moreover, higher nanoparticle concentrations result in lower σ_i values. At the U-bend section, the combination of the twisted structure and 5 % Cu MSBN reduces the two σ_i peaks from 9.88×10^{-4} and 13.73×10^{-4} in the smooth tube to 8.32×10^{-4} and 5.45×10^{-4}, respectively. This indicates that the synergistic effect of the twisted tube and nanoparticles effectively mitigates extreme temperature non-uniformity along the tube

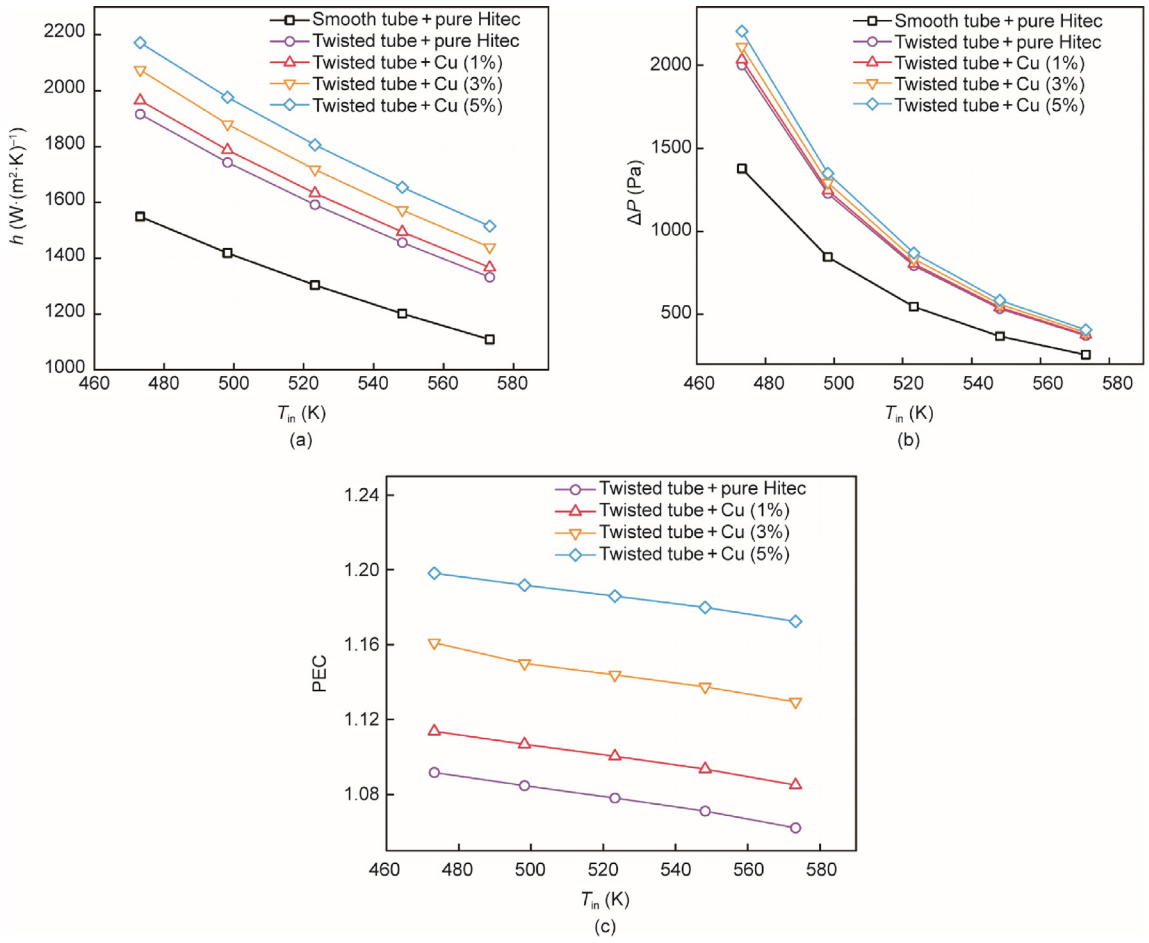

Fig. 13. Variations of (a) h, (b) ΔP, and (c) PEC with respect to T_{in} for molten salt fluids containing nanoparticles at different volume fractions in smooth and twisted tubes.

wall, thereby reducing the risk of tube rupture and molten salt decomposition.

4.3.2. Effect of Reynolds number

Figs. 16(a) and (b) present the effects of different *Re* on h_i and σ_i along the flow direction in a twisted U-tube containing 5% Cu MSBN, under conditions of q = 60 kW·m^{-2} and T_{in} = 523.15 K. The analysis reveals that the rate of increase in h_i within the U-bend section rises with increasing *Re*. This is attributed to enhanced turbulence intensity, which disrupts the thermal boundary layer and promotes more effective fluid mixing. At *Re* values of 4 000, 8 000, and 12 000, the maximum h_i values are 1781.52, 2753.04, and 3611.42 W·(m^2·K)$^{-1}$, respectively. This phenomenon demonstrates that secondary flow significantly enhances local heat transfer performance in the U-bend section under high turbulence conditions.

Fig. 16(b) illustrates that increasing the *Re* improves temperature uniformity within the TCUT. As *Re* increases from 4 000 to 12 000, the peak σ_i decreases from 0.00140 to 0.00041, with both the fluctuation and growth rate of σ_i in the U-bend section being significantly reduced. This indicates that operation at higher *Re* is more effective in mitigating localized high-temperature regions caused by the curved geometry.

4.3.3. Effect of inlet temperature

Figs. 17(a) and (b) illustrate the effects of different T_{in} on h_i and σ_i along the flow direction in the TCUT containing 5 % Cu MSBN, under conditions of q = 60 kW·m^{-2} and *Re* = 6000. As depicted in Fig. 17(a), the growth rate of h_i in the U-bend section decreases with increasing T_{in}. This is because the MSBN has a higher mass flow rate and turbulence intensity at lower T_{in} under the same *Re*. At T_{in} values of 473.15, 523.15, and 573.15 K, the maximum h_i values are 2771.56, 2303.69, and 1911.09 W·(m^2·K)$^{-1}$, respectively, indicating that secondary flow significantly enhances heat transfer in the U-bend section at lower T_{in}.

Fig. 17(b) demonstrates that lower T_{in} is beneficial for reducing both the average and fluctuation of σ_i in the TCUT. As T_{in} increases from 473.15 to 573.15 K, the peak σ_i value rises from 0.00099 to 0.00071, and the growth rate of σ_i in the U-bend section decreases with decreasing T_{in}. This suggests that operation at lower T_{in} is more advantageous for mitigating circumferential temperature non-uniformity caused by the curved structure.

4.4. Multi-objective optimization

4.4.1. RSM analysis

This study employs RSM combined with NSGA-II to optimize operating conditions. Based on the aforementioned analysis, it is evident that increasing the nanoparticle volume fraction within the range of 0–5% can effectively enhance the overall heat transfer performance. However, when the nanoparticle concentration exceeds this threshold, the likelihood of nanoparticle aggregation and sedimentation in the base fluid increases significantly [44]. Therefore, all subsequent research cases will focus on 5% Cu MSBN. A two-factor, three-level RSM experiment was designed using the central composite design (CCD) approach. The *Re* and T_{in} of the MSBN were selected as independent variables, while the convective heat transfer coefficient (h), pressure drop (ΔP), and maximum

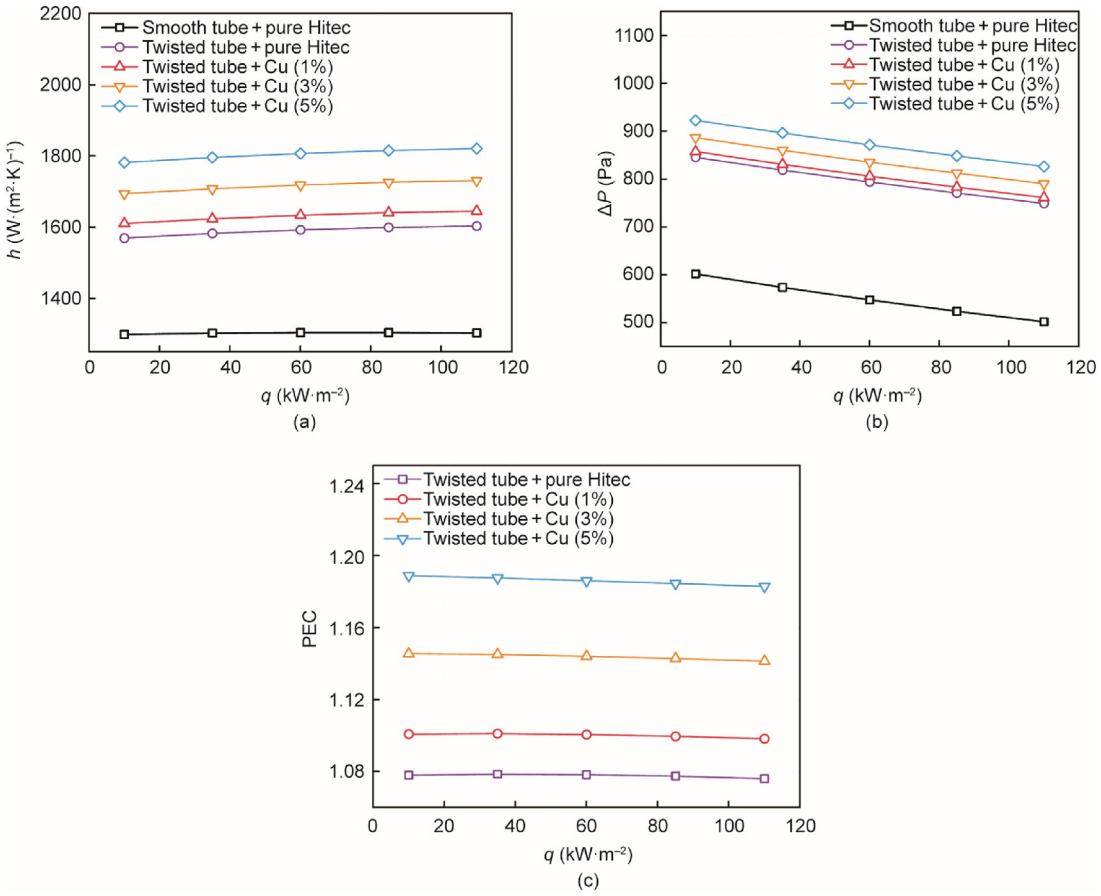

Fig. 14. Variations of (a) h, (b) ΔP, and (c) PEC with respect to q for molten salt fluids containing nanoparticles at different volume fractions in smooth and twisted tubes.

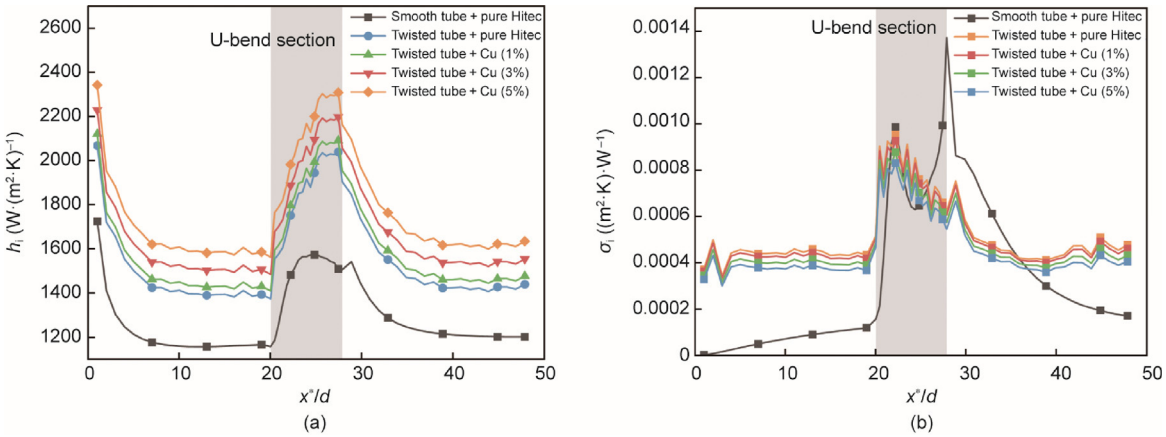

Fig. 15. Changes of (a) h_i and (b) σ_i along the flow direction under the influence of diverse structures and nanoparticles.

temperature difference (ΔT_{max}) were defined as response variables. Table 3 illustrates the case and simulation results based on the RSM design.

The highest order of the RSM directly affects the fitting ability and applicability of the model. Increasing the highest order can enhance the nonlinear fitting ability, but it also increases the risk of overfitting. After conducting residual analysis and prediction error tests, the fitness functions of ΔT_{max} and h were determined to be 2, and that of ΔP was 3. The fitting functions are as follows:

$$\Delta T_{max} = 70.92745 - 0.031294Re + 0.28502T_{in} + 0.00000130623Re^2 \quad (28)$$

$$\Delta P = -52294.6703 + 20.95297Re + 175.86554T_{in} - 0.070808Re \cdot T_{in} - 0.000084Re^2 - 0.145461T_{in}^2 + 0.000000185301Re^2 \cdot T_{in} + 0.000059Re \cdot T_{in}^2 \quad (29)$$

$$h = 7100.08784 + 0.584275Re - 22.75629T_{in} - 0.000638Re \cdot T_{in} - 0.00000293254Re^2 + 0.018989T_{in}^2 \quad (30)$$

Figs. 18(a)–(c) present the interactive effects of the Re and T_{in} on the ΔT_{max}, ΔP, and h within the TCUT. It can be observed that higher Re values combined with lower T_{in} values lead to an increase in h and a decrease in ΔT_{max}, while also causing a

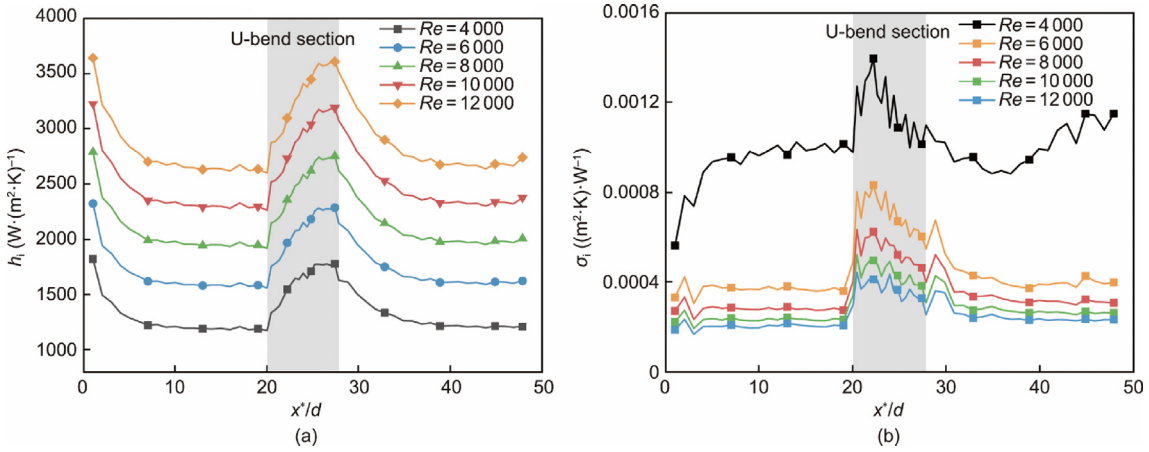

Fig. 16. Changes of (a) h_i and (b) σ_i along the flow direction under the influence of different *Re*.

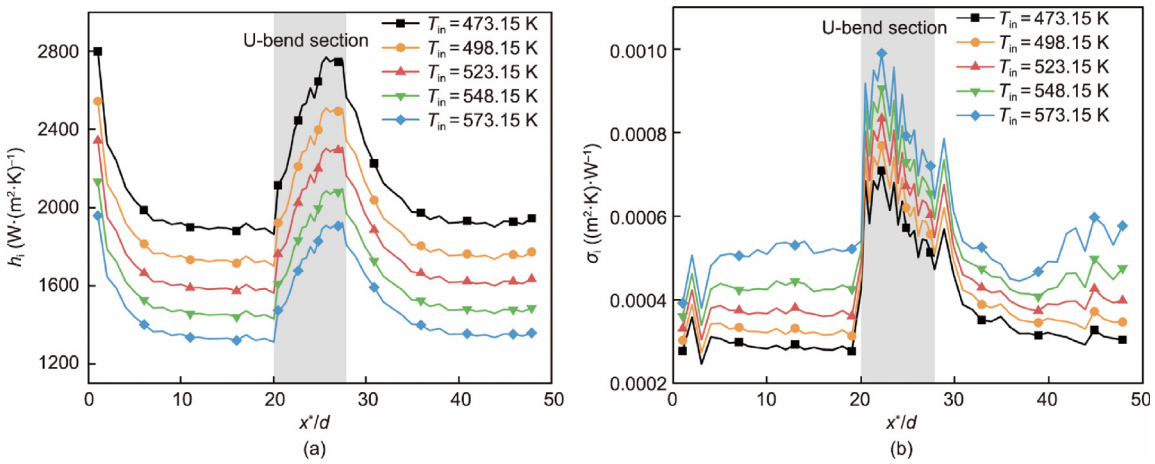

Fig. 17. Changes of (a) h_i and (b) σ_i along the flow direction under the influence of different T_{in}.

Table 3
Case design and simulation results.

Run	Factor		Response		
	Re	T_{in} (K)	ΔT_{max} (K)	ΔP (Pa)	h (W·(m²·K)⁻¹)
1	13 656.90	523.15	54.44	3462.54	2208.19
2	4 000.00	473.15	34.86	1128.13	3265.61
3	4 000.00	573.15	130.41	208.21	1729.93
4	8 000.00	523.15	54.44	1409.21	959.64
5	12 000.00	473.15	45.89	7024.88	1664.88
6	8 000.00	523.15	42.32	1409.21	1129.70
7	12 000.00	573.15	54.44	1310.11	2208.19
8	8 000.00	523.15	54.44	1409.21	2208.19
9	8 000.00	523.15	165.66	1409.21	2208.19
10	8 000.00	593.86	81.43	502.69	2500.84
11	2 343.15	523.15	68.81	185.72	2872.88
12	8 000.00	452.44	54.44	5613.41	3546.46
13	8 000.00	523.15	18.31	1409.21	2208.19

significant rise in ΔP. The analysis indicates that the influence of *Re* on ΔT_{max} and h is considerably greater than that of T_{in}, whereas both parameters exert similar effects on ΔP.

Based on the preceding response surface analysis, it is evident that a trade-off relationship exists among ΔT_{max}, ΔP, and h. Simultaneously minimizing ΔT_{max} and ΔP while maximizing h to the greatest extent possible is most favorable for the efficient operation of molten salt heat exchangers. This study proposes the application of the NSGA-II algorithm for multi-objective optimization, aiming to identify the optimal operating conditions based on the established response surface model. As a widely adopted multi-objective optimization algorithm, NSGA-II improves upon the original NSGA by addressing its limitations in computational efficiency and parameter dependency through the incorporation of fast non-dominated sorting, crowding distance comparison, and elitism preservation mechanisms.

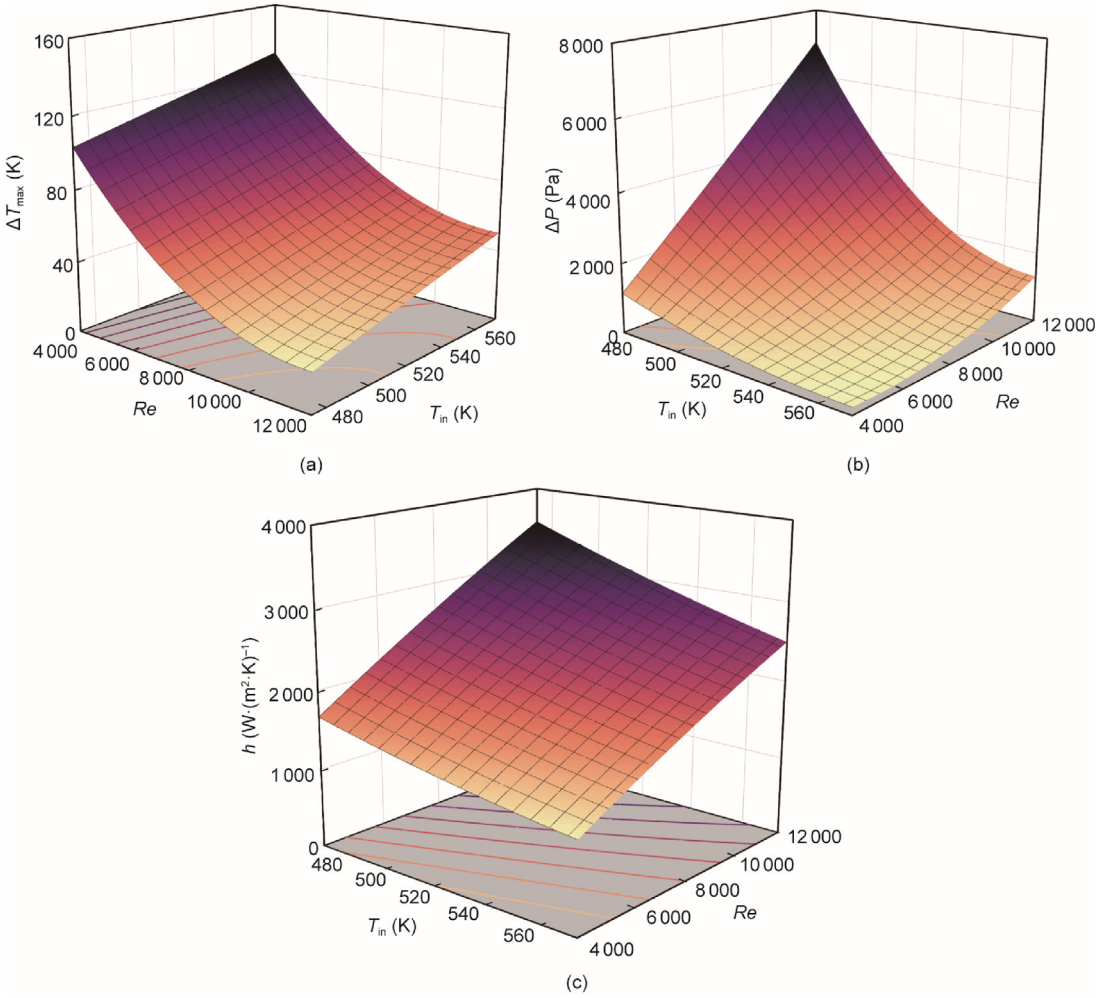

Fig. 18. Three-dimensional response surface: (a) ΔT_{max}, (b) ΔP, and (c) h.

4.4.2. Comprehensive optimization based on NSGA-II

This study utilizes the NSGA-II algorithm to compute the Pareto front based on the equations derived through RSM. The mathematical formulation of the optimized model is presented as follows:

$$\begin{cases} \text{Minimize} : \Delta T_{\max} = \Delta T_{\max}(Re, T_{\text{in}}) \\ \text{Minimize} : \Delta P = \Delta P(Re, T_{\text{in}}) \\ \text{Maximum} : h = h(Re, T_{\text{in}}) \\ \text{Subject to} : \\ Re \in [4\,000, 12\,000], T_{\text{in}} \in [473.15, 573.15] \end{cases} \tag{31}$$

In the NSGA-II algorithm, the initial population size is set to 100, with a maximum iteration count of 500 and a fitness function convergence threshold of 10^{-4}. The Pareto front obtained through iterative computation is presented in Fig. 19. Each point on the curve represents a non-dominated solution, meaning it cannot be outperformed by any other solution across all objective functions. The ideal point in Fig. 19 corresponds to the minimum ΔT_{max}, ΔP, and maximum h, with respective values of 21.85 K, 204.02 Pa, and 3550.23 W·(m^2·K)$^{-1}$, indicating that all objective functions have reached their optimal values. The equilibrium point is defined as the solution on the Pareto front with the shortest normalized distance to the ideal point. This solution corresponds to Re and T_{in} values of 11 713.23 and 537.25 K, respectively. Under these operating conditions in the TCUT, the resulting ΔT_{max}, ΔP, and h values are 40.15 K, 1979.97 Pa, and 2781.31 W·(m^2·K)$^{-1}$, respectively, with a PEC of 1.1475. Validation of the selected solution via Fluent simulations revealed relative errors of 3.23% for ΔT_{max}, 7.03% for ΔP, and 0.27% for h, confirming the reliability of the Pareto front optimization results.

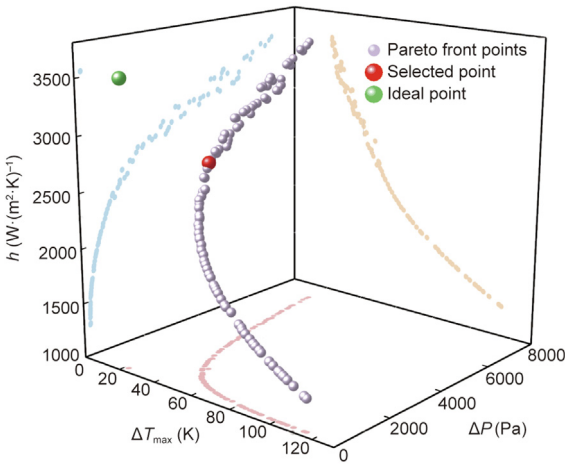

Fig. 19. Pareto frontier curve based on NSGA-II optimization.

5. Conclusions

In this study, a novel approach integrating a TCUT structure with nanoparticle addition is proposed to address the challenges

of localized high temperatures and non-uniform wall temperature distribution in molten salt flow within U-tube heat exchangers. The research investigates the effects of U-tube geometry, nanoparticle properties, and operational parameters on the heat transfer and flow performance of MSBN. The RSM and the NSGA-II algorithm are applied to identify the optimal operational parameters. The key findings are summarized as follows:

(1) When molten salt flows through a smooth U-tube, the combined effects of centrifugal and buoyancy forces generate significant secondary flow in the U-bend section and outlet section, resulting in the formation of local high-temperature zones. The cloverleaf twisted structure can induce up to four vortices in the U-bend section, enhancing the mixing of hot and cold fluids. This twisted configuration effectively improves the uniformity of temperature distribution, reducing the peak temperature and maximum temperature difference at the U-bend section.

(2) Among the three tested nanofluids, Cu MSBN achieves the lowest pressure drop while maintaining favorable heat transfer performance. Within the studied range, a 5% Cu MSBN combined with the TCUT configuration can reach a maximum PEC of 1.21.

(3) Inlet temperature and Reynolds number have a significant impact on both the heat transfer and pressure drop characteristics of molten salt and MSBN in the TCUT. Variations in heat flux primarily affect the pressure drop, while the convective heat transfer coefficient and PEC remain relatively less affected.

(4) The convective heat transfer coefficient of MSBN exhibits an initial increase followed by a decrease when passing through the U-bend section. The twisted structure significantly enhances the growth rate of the local convective coefficient within the bend. The peak local convective heat transfer coefficient decreases with increasing inlet temperature but increases with higher *Re* and nanoparticle volume fraction.

(5) The Pareto front obtained through the NSGA-II algorithm identifies the optimal operating conditions for 5% Cu MSBN in the modified structure as a *Re* of 11 713.23 and a T_{in} of 537.25 K. Under this condition, the maximum temperature difference, pressure drop, and average convective heat transfer coefficient are 40.15 K, 1979.97 Pa, and 2781.31 $W\cdot(m^2\cdot K)^{-1}$, respectively.

CRediT authorship contribution statement

Yifan Gui: Writing – original draft, Validation, Data curation. **Yuanqiang Duan:** Writing – review & editing, Writing – original draft, Methodology, Funding acquisition. **Shuo Zhang:** Writing – review & editing, Writing – original draft, Methodology, Data curation. **Yu Huang:** Writing – review & editing. **Minmin Zhou:** Writing – review & editing, Methodology. **Lunbo Duan:** Writing – review & editing, Supervision, Conceptualization.

Declaration of competing interest

The authors declare that they have no known competing financial interests or personal relationships that could have appeared to influence the work reported in this paper.

Acknowledgments

This work was supported by Jiangsu Province Science Foundation for Youths (BK20210238) and Jiangsu Provincial Carbon Peak & Carbon Neutrality Science and Technology Innovation Special Fund (BE2023094-3).

Appendix A. Supplementary data

Supplementary data to this article can be found online at https://doi.org/10.1016/j.eng.2025.10.010.

References

[1] Luo Z, Yang S, Xie N, Xie W, Liu J, Agbodjan Y, et al. Multi-objective capacity optimization of a distributed energy system considering economy, environment and energy. Energy Convers Manage 2019;200:112081.
[2] Wu Y, Fu L, Zhang S, Tang D. Study on a novel co-operated heat and power system for improving energy efficiency and flexibility of cogeneration plants. Appl Therm Eng 2019;163:114429.
[3] Liu B, Gao W, Li Q, Chen H, Zhang Y, Ding X. Quantification of thermal stratification and its impact on energy efficiency in solar hot water storage tanks. Energy 2025;326:136243.
[4] Abedigamba O, Mndeme F, Mawire A, Bahadur I. Thermo-physical properties and thermal energy storage performance of two vegetable oils. J Energy Storage 2023;61:106774.
[5] Kearney D, Kelly B, Herrmann U, Cable R, Pacheco J, Mahoney R, et al. Engineering aspects of a molten salt heat transfer fluid in a trough solar field. Energy 2004;29(5–6):861–70.
[6] Sayoud N, Yüksel A, Laouer A, Teggar M, Arıcı M, Brihi N. Numerical investigation of thermal energy storage characteristics of dual phase change material in double elliptic pipe. Int Commun Heat Mass Transf 2025;164:108921.
[7] Xue X, Niu Z, Zheng L, Xu G, Cao H, Wang Y. Design and performance analysis of a coal-fired power plant integrated with high and low temperature molten salt thermal storage for improving peaking capacity. Energy 2025;331:137106.
[8] Wang W, Li M, Cheng Z, Li D, Liu Z. Coupled optical–thermal–stress characteristics of a multi-tube external molten salt receiver for the next generation concentrating solar power. Energy 2021;233:121110.
[9] Wang J, Zhai Y, Wang H, Li Z. Heat transfer performance of supercritical R134a in a U-bend vapor generator for transcritical ORC system. Energy 2023;276:127520.
[10] Wang Y, Ren J, Gao W, Zhang J, Yu G, Bi M. Mechanism analysis on heat transfer of supercritical LNG in horizontal U-bend tube. Energy 2024;304:131936.
[11] He Y, Guo X, Li Z, Zhai Y. Heat transfer characteristics of supercritical R134a in micro-fin tubes. Int J Therm Sci 2025;215:109943.
[12] Szydłowski M, Gutkowski A. Numerical analysis of heat exchanger with inclined finned semicircular tubes. Int Commun Heat Mass Transf 2025;160:108326.
[13] Frantz C, Buck R, Röger M, Hoffschmidt B. Experimental analysis of forced convective heat transfer of nitrate salt in a spirally grooved tube at high Reynolds numbers and temperatures. Int J Heat Mass Transf 2023;204:123834.
[14] Gao Y, Wang X, Xu M, Hu Q, Ghoreishi-Madiseh SA, Aziz M. Investigation of heat transfer characteristics of nanofluid ice slurry flowing in spiral bellows. Int Commun Heat Mass Transf 2024;156:107583.
[15] Zhang Y, Zheng S, Meng J, Shi H, Yang Y, Li H, et al. Thermal–hydraulic performances and characteristics of hierarchical rib arrangements in serpentine cooling channels. Appl Therm Eng 2025;264:125481.
[16] Mehta B, Subhedar D, Panchal H, Said Z, Sharma K, Irfanul Haque Siddiqui M, et al. Twisted tape inserts in parabolic trough solar collectors: assessment of energy, exergy, and environmental impacts. Appl Therm Eng 2024;250:123566.
[17] Joo H, Kwak H, Kong M. Effect of twisted tape inserts on thermal performance of heat pipe evacuated-tube solar thermal collector. Energy 2022;254:124307.
[18] Saini P, Dhar A, Powar S. Performance evaluation of a parabolic trough collector with a uniform helical wire coil flow insert. Results Eng 2024;21:101794.
[19] Guo A, Wang L. The mechanism of laminar convective heat transfer enhancement enforced by twisting of elliptical tube. Int J Heat Mass Transf 2020;157:119961.
[20] Bhadouriya R, Agrawal A, Prabhu S. Experimental and numerical study of fluid flow and heat transfer in a twisted square duct. Int J Heat Mass Transf 2015;82:143–58.
[21] Li X, Chen S, Tan Y, Sun Z, Tian G, Wang L. Convective thermal–hydraulic performance in twisted tubes: from the perspective of symmetrical cross-sectional shapes. Int Commun Heat Mass Transf 2023;147:106974.
[22] Eiamsa-ard S, Maruyama N, Hirota M, Skullong S, Promthaisong P. Heat transfer mechanism in ribbed twisted-oval tubes. Int J Therm Sci 2023;193:108532.
[23] Wang M, Li X, Tan Y, Wang L, Peng Y, Wang Z. Convective heat transfer enhancement by combination effect of twist and helix in helical twisted tubes. Therm Sci Eng Prog 2025;60:103504.
[24] Han Y, Wu Y, Meng F, Zhang C, Wu Y, Wu X, et al. Multi-objective optimization study on heat transfer performance of solar salt in non-circular twisted tube heat exchanger based on entropy generation number and NSGA II. Int J Therm Sci 2025;211:109681.
[25] Ying Z, He B, Su L, Kuang Y, He D, Lin C. Convective heat transfer of molten salt-based nanofluid in a receiver tube with non-uniform heat flux. Appl Therm Eng 2020;181:115922.
[26] Ying Z, He B, Su L, Kuang Y. Thermo–hydraulic analyses of the absorber tube with molten salt-based nanofluid and porous medium inserts. Sol Energy 2021;226:20–30.
[27] Kaood A, Abubakr M, Al-Oran O, Hassan M. Performance analysis and particle swarm optimization of molten salt-based nanofluids in parabolic trough concentrators. Renew Energy 2021;177:1045–62.

[28] Zhang C, Han S, Wu Y, Zhang C, Guo H. Investigation on convection heat transfer performance of quaternary mixed molten salt based nanofluids in smooth tube. Int J Therm Sci 2022;177:107534.
[29] Shih T, Liou W, Shabbir A, Yang Z, Zhu J. A new k–ϵ eddy viscosity model for high Reynolds number turbulent flows. Comput Fluids 1995;24(3):227–38.
[30] Carloni ACN, Conde KE, Pantaleão AV, Azevedo JLF, Rade DA. Validation and analysis of turbulence modeling in pipe elbow under secondary flow conditions. J Braz Soc Mech Sci Eng 2022;44(12):595.
[31] de Figueiredo LD, Boon J, Rodriguez GO, van Sint AM. Review of the molten salt technology and assessment of its potential to achieve an energy efficient heat management in a decarbonized chemical industry. Chem Eng J 2024;498:155819.
[32] Pak B, Cho Y. Hydrodynamic and heat transfer study of dispersed fluids with submicron metallic oxide particles. Exp Heat Transf 1998;11(2):151–70.
[33] Brinkman H. The viscosity of concentrated suspensions and solutions. J Chem Phys 1952;20(4):571.
[34] Chen H, Zhai Y, Huang H, Li Z, Wang H. Optimization of thermal resistance and thermal deformation in high heat-load zone of blast furnace cooling staves. Appl Therm Eng 2025;271:126292.
[35] Alhulaifi A. Numerical characterization of the performance of counter-flow double-pipe heat exchanger using nanofluids for laminar flow regime. Results Eng 2025;25:104061.
[36] Sanga PJ, Datta P, Kumar A. Effect of Brinkman and Maiga's correlations of viscosity on forced convection turbulent flow. Int Commun Heat Mass Transf 2024;159:108367.
[37] Qi C, Wan Y, Li C, Han D, Rao Z. Experimental and numerical research on the flow and heat transfer characteristics of TiO_2–water nanofluids in a corrugated tube. Int J Heat Mass Transf 2017;115:1072–84.
[38] Guo Z, Li D, Wang B. A novel concept for convective heat transfer enhancement. Int J Heat Mass Transf 1998;41(14):2221–5.
[39] Rogers G, Mayhew Y. Heat transfer and pressure loss in helically coiled tubes with turbulent flow. Int J Heat Mass Transf 1964;7(11):1207–16.
[40] Schmidt E. Wärmeübergang und druckverlust in rohrschlangen. Chemieingenieurtechnik 1967;39(13):781–9.
[41] Chen X, Wang C, Wu Y, Liu B, Ma C. Characteristics of the mixed convection heat transfer of molten salts in horizontal square tubes. Sol Energy 2017;147:248–56.
[42] Ho MX, Pan C. Experimental investigation of heat transfer performance of molten HITEC salt flow with alumina nanoparticles. Int J Heat Mass Transf 2017;107:1094–103.
[43] Lu Y, Zhi Y, Lu X, Yang B, Yu X. Heat transfer characterization of dish solar collector based on Al_2O_3 nanofluid. Appl Therm Eng 2025;277:127000.
[44] Liao J, Zhang A, Qing S, Zhang X, Luo Z. Investigation on the aggregation structure of nanoparticle on the thermal conductivity of nanofluids by molecular dynamic simulations. Powder Technol 2022;395:584–91.